AIAA JOURNAL
Vol. 41, No. 4, April 2003

Two-Dimensional Model for Simulating Shock-Wave Interaction with Rigid Porous Materials

G. Malamud,* D. Levi-Hevroni,† and A. Levy†
Ben-Gurion University of the Negev, 84105 Beer-Sheva, Israel

A two-dimensional numerical model for predicting the characteristics of the flowfield during an unsteady interaction between a shock wave moving through air and a rigid saturated porous matrix is developed. The numerical model includes a Lagrangian scheme combined with a remesh and an interface tracking technique. The predictions of the numerical simulations are compared with the predictions of a two-dimensional analytical model for regular reflection from a rigid porous surface in pseudosteady flow. The numerical and the physical model are also validated by comparing the one- and two-dimensional predictions of the model with experimental results. In general the predictions of the numerical simulations reveal very good to excellent agreement with both the experimental results and the predictions of the analytical model.

Nomenclature

C_α	=	specific heat capacities ratio for the α phase
c_α	=	shape factor for the α phase
$\boldsymbol{D}^{*H}$	=	dispersive heat tensor
e	=	specific internal energy
$\bar{e}_\alpha^\alpha$	=	average of intensive quality for the α phase
F	=	isotropic macroscopic Forchheimer coefficient
g	=	specific gravity
P	=	pressure
R	=	specific gas constant
S	=	interface between phases
$\boldsymbol{S}$	=	source vector
T	=	temperature
$\boldsymbol{T}_\alpha^*$	=	tortuosity tensor of an α phase
t	=	time
$\bar{\boldsymbol{u}}$	=	velocity vector
V	=	volume
V_0	=	representative elementary volume concept (REV)
x_i	=	unit vector in the ith direction
$\mathring{x}_i$	=	coordinate of a point in the REV relative to the REV center in the ith direction
α^{*H}	=	convection heat-transfer coefficient
Δ_g	=	hydraulic radius of the pores
ε_{sk}	=	volumetric strain
$\boldsymbol{\varepsilon}_{sk}$	=	strain tensor
$\bar{\eta}, \bar{\lambda}_s'^s, \bar{\mu}_s''^s$	=	Lame's constants for a thermoelastic solid matrix
λ_α^α	=	thermal conductivity for an alpha phase
$\boldsymbol{\xi}$	=	unit vector perpendicular to the REV surface
ρ	=	density
σ_s'	=	effective stress of the solid phase
ϕ_α	=	volumetric fraction of an α phase

Subscripts

g	=	gas
i, j, k	=	unit vectors in the orthogonal space coordinate system
s	=	solid
α	=	alpha phase

Received 7 March 2002; revision received 1 October 2002; accepted for publication 5 October 2002.

*Graduate Student, Pearlstone Center for Aeronautical Engineering Studies, Department of Mechanical Engineering.

†Senior Lecturer, Pearlstone Center for Aeronautical Engineering Studies, Department of Mechanical Engineering.

I. Introduction

THE reflection phenomenon of shock waves over different geometries and the interaction phenomenon of shock or compression waves with porous media are two phenomena that have gained much attention in the past two decades because of their application to many engineering fields. Although the reflection phenomenon and the head-on interaction of shock waves with porous media have reached a state where, from an engineering point of view, they are quite well understood and as such summarized in a few reviews and books,[1,2] the reflection phenomenon over different porous bodies is still under intensive investigation by many researchers because it is still far from being understood. Many models were developed in order to reach such an understanding.[3–8] The investigations on the interactions of shock waves with porous media were conducted with two types of porous materials, that is, compressible or rigid porous materials. A comprehensive study of such interactions was conducted in the Mechanical Engineering Department at the Ben-Gurion University of the Negev, Israel. The physical approach was summarized in Ref. 5 and 9 for the interaction with rigid porous materials and in Ref. 10 for the interaction with compressible foams. All of the theoretical models that were developed during those studies showed a very good agreement with the experimental results. Levy et al.[6] solved analytically the nonisothermal one-dimensional case of such an interaction and again reached a very good agreement with the experimental results of Ref. 11. Levy et al.[7] investigated numerically the head-on interaction of a shock wave with a saturated rigid porous material. An analytical model and a one-dimensional computer code were developed. The predictions of the numerical simulations were successfully compared with experimental results and validated both the physical model and the computer code.

When an oblique shock wave interacts with a porous layer, two types of wave configurations can be obtained above the porous layer. These types of wave configurations are known as regular reflection (RR) and irregular reflection (IR). The latter can be separated again, for von Newman reflection and Mach reflection (MR). Both types of wave configurations have well-known solutions when the oblique shock wave interacts with a solid wall. However, when it interacts with a porous layer the gaseous phase can penetrate into the porous layer and modify the wave configurations. Furthermore, additional waves and discontinuities can develop inside the porous layer (e.g., a transmitted oblique shock or compression wave and a slipstream).

Kobayashi et al.[12] proposed two different analytical models for describing the RR phenomenon. Then they solved the less realistic analytical model, where the coupling between the pure gas and the porous layer was neglected. Their more realistic model for the RR wave configuration (see Fig. 1) was analyzed and solved by Li et al.[13]

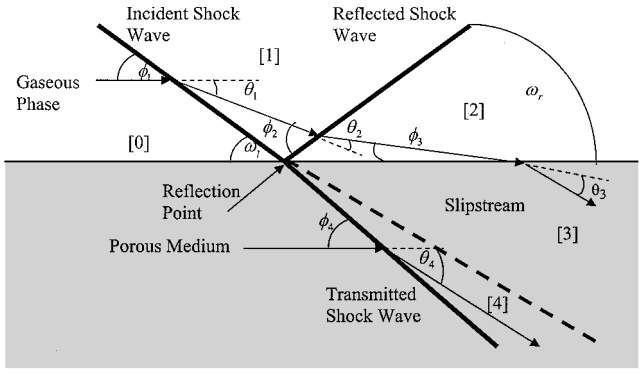

Fig. 1 Physical model for a RR.[12] State [0] is ahead of the incident and transmitted shock waves; state [1] is behind the incident shock wave; state [2] is behind the reflected shock wave; and state [4] is behind the transmitted shock wave. State [3] is obtained from state [2] when the flow penetrates the porous material. States [3] and [4] are separated by the contact discontinuity.

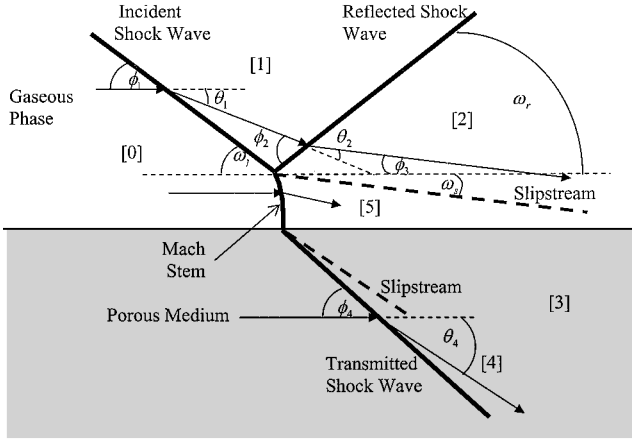

Fig. 2 Schematic illustration of the proposed wave configuration of a MR over a rigid porous layer. State [0] is ahead of the incident and transmitted shock waves; state [1] is behind the incident shock wave; state [2] is behind the reflected shock wave; state [4] is behind the transmitted shock wave; and state [5] is behind the Mach stem. State [3] is obtained from state [5] when the flow penetrates the porous material. States [3] and [4] are separated by the contact discontinuity inside the porous material, and states [2] and [5] are separated by the contact discontinuity, which starts at the triple point.

The more realistic model for a regular reflection wave configuration over a rigid porous media is shown in Fig. 1. In this model an incident shock wave that moves relative to the porous layer collides with the porous interface and generates two shock waves: the first is the reflected shock wave, which is the product of the solid phase interaction with the gas, and the second is a transmitted shock wave into the gaseous phase inside the porous layer. In addition, because of the transfer of mass into the porous layer a contact discontinuity is formed.

An analytical model for solving the flowfield associated with regular reflections of oblique shock waves over rigid porous layers was developed by Li et al.[13] The governing equations of the gaseous phase inside the porous layer were similar to those of the gaseous phase outside the porous layer as a result of a suggested transformation for macroscopic balance equations, which were obtained by an averaging process over a representative elementary volume of the microscopic balance equations. Based on this transformation, a model for estimating the tortuosity factor was obtained. The predictions of the analytical model were validated by comparing them to the experimental data of Refs. 12 and 14. The analytical model solved a set of 17 governing equations and could predict the properties of the fluid phase, along with the angles of the reflection and the diversion of the fluid velocity vectors from the shock waves and the porous surface. The sonic criterion together with the analytical model was used to predict the transition between the regular and the Mach reflections.

One proposed model for a Mach reflection wave configuration is shown in Fig. 2. In this figure a Mach stem and a slipstream are formed outside the porous medium. In this case at least one uniform flow zone has been formed. Because of that, the physical description of the MR is much more complicated then that of the RR. The MR contains five or more uniform flow zones instead of the four shown in the RR wave configuration. To the best of the authors' knowledge, no simplified analytical model has been published yet because the physical phenomenon of the Mach reflection over a porous layer is not yet fully understood. In addition, there has not been a comprehensive numerical or experimental study that confirmed the overall wave configuration as presented in Fig. 2. The main problem with regards to the wave configuration shown in Fig. 2 is related to the slipstream outside of the porous layer. The slipstream outside of the porous layer might be developed in three different ways. It can be parallel to the porous interface, oriented toward the porous interface, or oriented away from the porous interface. In addition, it is not known whether the slipstream interacts with the porous interface, and if it does, then how it interacts with the porous layer. Hence, it is very difficult to develop an analytical model for a Mach reflection over a porous layer. Motivated by these reasons and encouraged by the good results achieved by us so far, we felt confident enough to move forward and to develop a two-dimensional model in order to predict the flowfield characteristics of various two-dimensional reflection phenomena.

II. Theoretical Model

A detailed investigation of the shock-wave interaction with rigid porous materials was initiated on the theoretical basis of the macroscopic balance equations. The governing macroscopic mass, momentum, and energy balance equations, for a saturated porous medium, were developed[5] by conducting a dimensional analysis on the macroscopic balance equations of Refs. 4 and 9. The physical model was based on conceptualizing the porous medium as a continuum composed of interacting solid and fluid phases (saturated porous media). Macroscopic physical laws expressing the mass, the momentum, and the energy balances for the fluid phase and the solid matrix were formulated on the basis of the representative elementary volume (REV) concept, presented by Ref. 15. The macroscopic balance equations were composed of averaged flux terms together with integrals of microscopic exchange flux terms at the solid/fluid interface.

Based on the averaging process, new macroscopic terms have been added to the macroscopic balance equations, namely, the tortuosity tensor and the Forchheimer term. The tortuosity tensor is associated with the matrix directional cosines, the hydraulic radius of the pore spaces, and the porosity that represents the volume fraction of the pores filled by the fluid. This macroscopic tensor reflects the microscopic configuration of the solid-fluid interface.

A. Averaging Rules

The averaging technique that has been used followed Ref. 15 for the case of a saturated two-phase porous medium of general local geometrical. The volumetric fraction of gas ϕ_g and the solid ϕ_s phases are defined by

$$\phi_g = V_g/V_0 \tag{1}$$

$$\phi_s = V_s/V_0 = 1 - \phi_g \tag{2}$$

where V_g and V_s are the volume of the gaseous and the solid phases in the REV, respectively, and V_0 is the total volume ($V_0 = V_g + V_s$) of the REV.

An average of an intensive quantity of the α phase e_α over the gas phase volume within the REV is given by

$$\bar{e}_g^g = \frac{1}{V_g}\int_{V_0} e_g \, \mathrm{d}v \tag{3}$$

V_g represents the volume of gas phase inside V_0. Corresponding average rules were defined for time and space derivatives, taking

into account both the changes in the average quantity $\bar{e}_g^g$ and the fluxes through the REV boundaries.

The average of time derivative was written by

$$\phi_g \overline{\frac{\partial e_g^g}{\partial t}} = \frac{\partial \phi_g \bar{e}_g^g}{\partial t} - \frac{1}{V}\int_{S_{gs}} e_g \bar{\boldsymbol{u}}\boldsymbol{\xi}\, \mathrm{d}S \tag{4}$$

where $\boldsymbol{u}$ is the velocity of the gas phase surface. The average of a spatial derivative is given by

$$\overline{\frac{\partial e_g^g}{\partial x_i}} = \frac{\partial \bar{e}_g^g}{\partial x_j} T^*_{gij} + \frac{1}{\phi_g V_0}\int_{S_{gs}} \mathring{x}_i \frac{\partial e_g}{\partial x_j}\xi_j \, \mathrm{d}S \tag{5}$$

The tortuosity tensor $\boldsymbol{T}^*_{gij}$ represents the microscopic configuration of the solid–gas interface and therefore is defined (for the case of monotonous pressure gradient) for the α phase by

$$\boldsymbol{T}^*_{\alpha ij} = \frac{1}{\phi_\alpha V_0}\int_{S_{\alpha\alpha}} \mathring{x}_i \xi_j \, \mathrm{d}S \tag{6}$$

B. Macroscopic Balance Equations

Applying the averaging rules such as those given by Eqs. (3–6) on the microscopic balance equations for a compressible Newtonian fluid and a thermoelastic solid and neglecting the dispersive flux terms, the macroscopic balance equations were obtained.

Gas and solid mass balance equations were, respectively,

$$\frac{\mathrm{D}}{\mathrm{D}t}\left(\phi_g \bar{\rho}_g^g\right) = -\phi_g \bar{\rho}_g^g \nabla \cdot \bar{\boldsymbol{u}}_g^g \tag{7}$$

$$\frac{\mathrm{D}}{\mathrm{D}t}\left(\phi_s \bar{\rho}_s^s\right) = -\phi_s \bar{\rho}_s^s \nabla \cdot \bar{\boldsymbol{u}}_s^s \tag{8}$$

Gas and porous medium momentum balance equations were, respectively,

$$\begin{aligned}\phi_g \bar{\rho}_g^g \frac{\mathrm{D}}{\mathrm{D}t}\left(\bar{\boldsymbol{u}}_g^g\right) &= -\phi \boldsymbol{T}^*_g \nabla \bar{P}^g - \phi_g \bar{\rho}_g^g \boldsymbol{g}\boldsymbol{T}^*_g \nabla Z \\ &+ \bar{\mu}_g^g\left[\nabla^2 \phi_g\left(\bar{\boldsymbol{u}}_g^g - \bar{\boldsymbol{u}}_s^s\right) + \nabla \cdot \left(\phi_g \nabla \bar{\boldsymbol{u}}_s^s\right)\right] \\ &+ \left(\bar{\mu}_g^g + \bar{\lambda}''^g\right)\left\{\nabla\left[\nabla\phi_g \cdot \left(\bar{\boldsymbol{u}}_g^g - \bar{\boldsymbol{u}}_s^s\right)\right] + \nabla\left(\phi_g \nabla \cdot \bar{\boldsymbol{u}}_s^s\right)\right\} \\ &- \bar{\mu}_g^g c_f \phi_g \boldsymbol{\alpha} \cdot \frac{\bar{\boldsymbol{u}}_g^g - \bar{\boldsymbol{u}}_s^s}{\Delta_g^2} - \frac{c_f}{2\Delta_g^2}\boldsymbol{F}\phi_g \bar{\rho}_g^g \left(\bar{\boldsymbol{u}}_g^g - \bar{\boldsymbol{u}}_s^s\right)\left(\bar{\boldsymbol{u}}_g^g - \bar{\boldsymbol{u}}_s^s\right)\end{aligned} \tag{9}$$

$$\begin{aligned}\phi_g \bar{\rho}_g^g \frac{\mathrm{D}}{\mathrm{D}t}\left(\bar{\boldsymbol{u}}_g^g\right) + \left(\phi_s \bar{\rho}_s^g\right)\frac{\mathrm{D}}{\mathrm{D}t}\left(\bar{\boldsymbol{u}}_s^s\right) &= -\left(\phi_g \bar{\rho}_g^g + \phi_s \bar{\rho}_s^s\right) g \nabla Z \\ &+ \frac{\bar{\mu}_g^g}{\phi_g}\left[\nabla^2 \phi_g\left(\bar{\boldsymbol{u}}_g^g - \bar{\boldsymbol{u}}_s^s\right) + \nabla\nabla \cdot \phi_g\left(\bar{\boldsymbol{u}}_g^g - \bar{\boldsymbol{u}}_s^s\right)\right] \\ &+ \frac{\bar{\lambda}_g''^g}{\phi_g}\nabla\nabla \cdot \phi_g \cdot \left(\bar{\boldsymbol{u}}_g^g - \bar{\boldsymbol{u}}_s^s\right) + \bar{\mu}_g^g\left(\nabla^2 \bar{\boldsymbol{u}}_s^s + \nabla\nabla \cdot \bar{\boldsymbol{u}}_s^s\right) \\ &+ \bar{\lambda}_g''^g \nabla\nabla \cdot \bar{\boldsymbol{u}}_s^s - \nabla \bar{\boldsymbol{P}}^g - \bar{\eta}\nabla \bar{T}_s^s + \bar{\mu}_s^s \nabla \cdot \boldsymbol{\varepsilon}_{\mathrm{sk}} + \bar{\lambda}_s''^s \nabla \varepsilon_{\mathrm{sk}}\end{aligned} \tag{10}$$

Gas and solid energy balance equations were, respectively,

$$\begin{aligned}\frac{\mathrm{D}}{\mathrm{D}t}\left\{\phi_g \bar{\rho}_g^g\left[C_g \bar{T}_g^g + \frac{\left(\bar{\boldsymbol{u}}_g^g\right)^2}{2}\right]\right\} &= \left\{\phi_g \bar{\rho}_g^g\left[C_g \bar{T}_g^g + \frac{\left(\bar{\boldsymbol{u}}_g^g\right)^2}{2}\right]\right\}\nabla \cdot \bar{\boldsymbol{u}}_g^g \\ &- \alpha^{*H}\left(\bar{T}_g^g - \bar{T}_s^s\right) + \boldsymbol{T}^*_g \bar{P}^g \bar{\boldsymbol{u}}_s^s \nabla \phi_g - \boldsymbol{T}^*_g \nabla\left(\phi_g \bar{P}^g \bar{\boldsymbol{u}}_g^g\right) \\ &+ \nabla \cdot \left[\phi_g \boldsymbol{D}^{*H} \nabla\left(C_g \bar{\rho}_g^g \bar{T}_g^g\right) + \phi_g \bar{\lambda}_g^g \nabla \bar{T}_g^g\right] \\ &- \left[\bar{\mu}_g^g c_f \phi_g \boldsymbol{\alpha} \cdot \frac{\bar{\boldsymbol{u}}_g^g - \bar{\boldsymbol{u}}_s^s}{\Delta_g^2} + \frac{c_f}{2\Delta_g^2}\boldsymbol{F}\phi_g \bar{\rho}_g^g\left(\bar{\boldsymbol{u}}_g^g - \bar{\boldsymbol{u}}_s^s\right)\left(\bar{\boldsymbol{u}}_g^g - \bar{\boldsymbol{u}}_s^s\right)\right]\bar{\boldsymbol{u}}_s^s\end{aligned} \tag{11}$$

$$\begin{aligned}\frac{\mathrm{D}}{\mathrm{D}t}\left\{\phi_s \bar{\rho}_s^s\left[C_s \bar{T}_s^s + \frac{\left(\bar{\boldsymbol{u}}_s^s\right)^2}{2}\right]\right\} &= \left\{\phi_s \bar{\rho}_s^s\left[C_s \bar{T}_s^s + \frac{\left(\bar{\boldsymbol{u}}_s^s\right)^2}{2}\right]\right\}\nabla \cdot \bar{\boldsymbol{u}}_s^s \\ &+ \alpha^{*H}\left(\bar{T}_g^g - \bar{T}_s^s\right) + \boldsymbol{T}^*_g \bar{P}^g \bar{\boldsymbol{u}}_s^s \nabla \cdot \left(\phi_s \bar{P}^g \bar{\boldsymbol{u}}_s^s\right) \\ &- \boldsymbol{T}^*_g \bar{P}^g \bar{\boldsymbol{u}}_s^s \nabla \phi_g - \nabla \cdot \left(\sigma'_s \bar{\boldsymbol{u}}_s^s\right) - \nabla \cdot \left[\phi_s \bar{\lambda}_s^s \nabla \bar{T}_s^s\right] \\ &+ \left[\bar{\mu}_g^g c_f \phi_g \boldsymbol{\alpha} \cdot \frac{\bar{\boldsymbol{u}}_g^g - \bar{\boldsymbol{u}}_s^s}{\Delta_g^2} + \frac{c_f}{2\Delta_g^2}\boldsymbol{F}\phi_g \bar{\rho}_g^g\left(\bar{\boldsymbol{u}}_g^g - \bar{\boldsymbol{u}}_s^s\right)\left(\bar{\boldsymbol{u}}_g^g - \bar{\boldsymbol{u}}_s^s\right)\right]\bar{\boldsymbol{u}}_s^s\end{aligned} \tag{12}$$

References 5 and 16 showed that the linear Darcy term was much smaller than the nonlinear Forchheimer term. Consequently, the linear Darcy term was not taken into account in the momentum and the energy exchanges between the two phases.

From hereafter we will refer to the macroscopic properties, and hence we will omit the sign of the average quantity (i.e., $\bar{e}^\alpha$).

C. Model Assumptions

A parametric study on the flowfield characteristics was conducted by Levy et al.[17] They showed that the main macroscopic physical properties that affected the gas flowfield characteristics were the Forchheimer and the tortuosity tensors and the gas and solid volume fractions. Based on the dimensional analysis of Ref. 5 on the macroscopic balance equations and the parametric study of Ref. 17, the following assumptions were considered during this study:

1) Perfect gas $P = \rho RT$.

2) Nonviscous and nonconducting fluid $\bar{\lambda}_g^g = \alpha^{*H} = 0$.

3) Two-dimensional flows.

4) The solid matrix is rigid (i.e., the solid density and porosity are constant, the solid velocity is zero, and therefore all of the balance equations of the solid phase have their trivial solutions).

5) The solid matrix is isotropic (i.e., uniform tortuosity and Forchheimer tensors in all directions).

6) Darcy's term is negligibly small compared to the Forchheimer term.

7) The dispersive and diffusive mass fluxes of the fluid are much smaller than the corresponding advective ones and might, therefore, be neglected.

8) The dispersive momentum flux of the fluid is much smaller than its advective one and can, therefore, be neglected.

9) The conductive and dispersive heat fluxes of the fluid are negligibly small when compared to its advective one.

10) The microscopic solid/fluid interface is a material surface with respect to the mass of both phases.

D. Balance Equations

Based on the assumptions just mentioned and in order to implement a Lagrangian numerical scheme, the macroscopic balance equations for the gaseous phase were rewritten in the following nonconservative form.

Continuity equation:

$$\frac{\mathrm{D}}{\mathrm{D}t}(\phi\rho) = -\phi\rho\nabla(\boldsymbol{u}) \tag{13}$$

Conservation of momentum equation:

$$\frac{\mathrm{D}\boldsymbol{u}}{\mathrm{D}t} = -\frac{T^*}{\rho}\nabla P + \boldsymbol{S} \tag{14}$$

Conservation of energy equation:

$$\frac{\mathrm{D}e}{\mathrm{D}t} = -T^*\phi P\,\frac{\mathrm{D}(V/\phi)}{\mathrm{D}t} + S_e \tag{15}$$

where $\boldsymbol{S}$ for the balance equations is

$$\boldsymbol{S} = \begin{pmatrix} -\tilde{F}|\boldsymbol{u}|u_x \\ -\tilde{F}|\boldsymbol{u}|u_y \end{pmatrix}, \qquad \phi \neq 1, \qquad \boldsymbol{S} = \begin{pmatrix} 0 \\ 0 \end{pmatrix}, \qquad \phi = 1 \tag{16}$$

$$S_e = \begin{cases} |\boldsymbol{u}|\tilde{F}\left(u_x^2 + u_y^2\right) & \phi \neq 1 \\ 0 & \phi \neq 1 \end{cases} \tag{17}$$

where $\tilde{F}(\equiv c_f/2\Delta_g^2\boldsymbol{F})$ is the isotropic macroscopic Forchheimer coefficient and u_x and u_y denote the velocity components in the x and y directions, respectively.

E. Complementary Equations

The equation of state to the gaseous phase is the standard equation for a perfect gas is

$$P = (\gamma - 1)e\rho \tag{18}$$

Here γ is the specific heat capacities ratio, which is defined by

$$\gamma = c_p/c_v \tag{19}$$

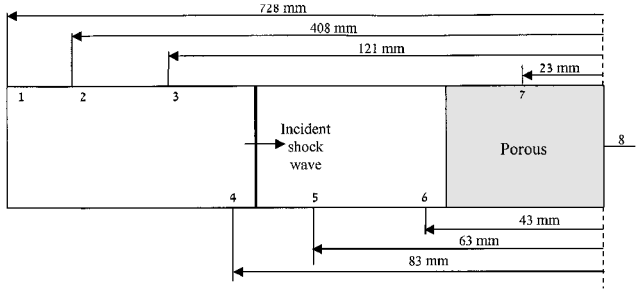

Fig. 3 Schematic illustration of the experimental setup and the location of eight pressure transducer ports.

III. Numerical Model

Since the invention of the computer and its introduction to the scientific world, numerous numerical schemes for solving the balance equations of a fluid were developed. In the present work a Lagrangian numerical scheme, originally developed by the authors of Ref. 18 for elastic plastic flows, was modified and extended to solve the two-dimensional interaction of a shock wave with a rigid porous material. The modification of the numerical scheme converts it into an arbitrary Lagrangian Eulerian (ALE) scheme and implemented an Eulerian remesh technique. Grid effects were examined by using a double grid resolution and conducting convergence checks. Very small-scale numerical changes were noticed, and no integrating effects on the solution were found to be evident.

The prediction of the flowfield characteristics for each time step is achieved by a Lagrangian solution of the balance equations. The solution of the Lagrange method is based on fixed mass elements located at the mesh vertices that can move in space. During each time step, a nonsymmetric movement of the vertices creates large strains. To avoid the large distortion of the Lagrangian mesh, the code projects all of the new physical properties into the original Eulerian grid. A detailed description of the numerical scheme is presented in the Appendix.

IV. Comparisons Between Numerical Predictions, Experimental Data, and Prediction of Analytical Models and Discussion

To validate the physical model and the numerical code, it was decided to compare the prediction of the numerical simulations with both available experimental data and predictions of analytical models. In the following section the assessment of the prediction of the numerical simulations for one- and two-dimensional cases will

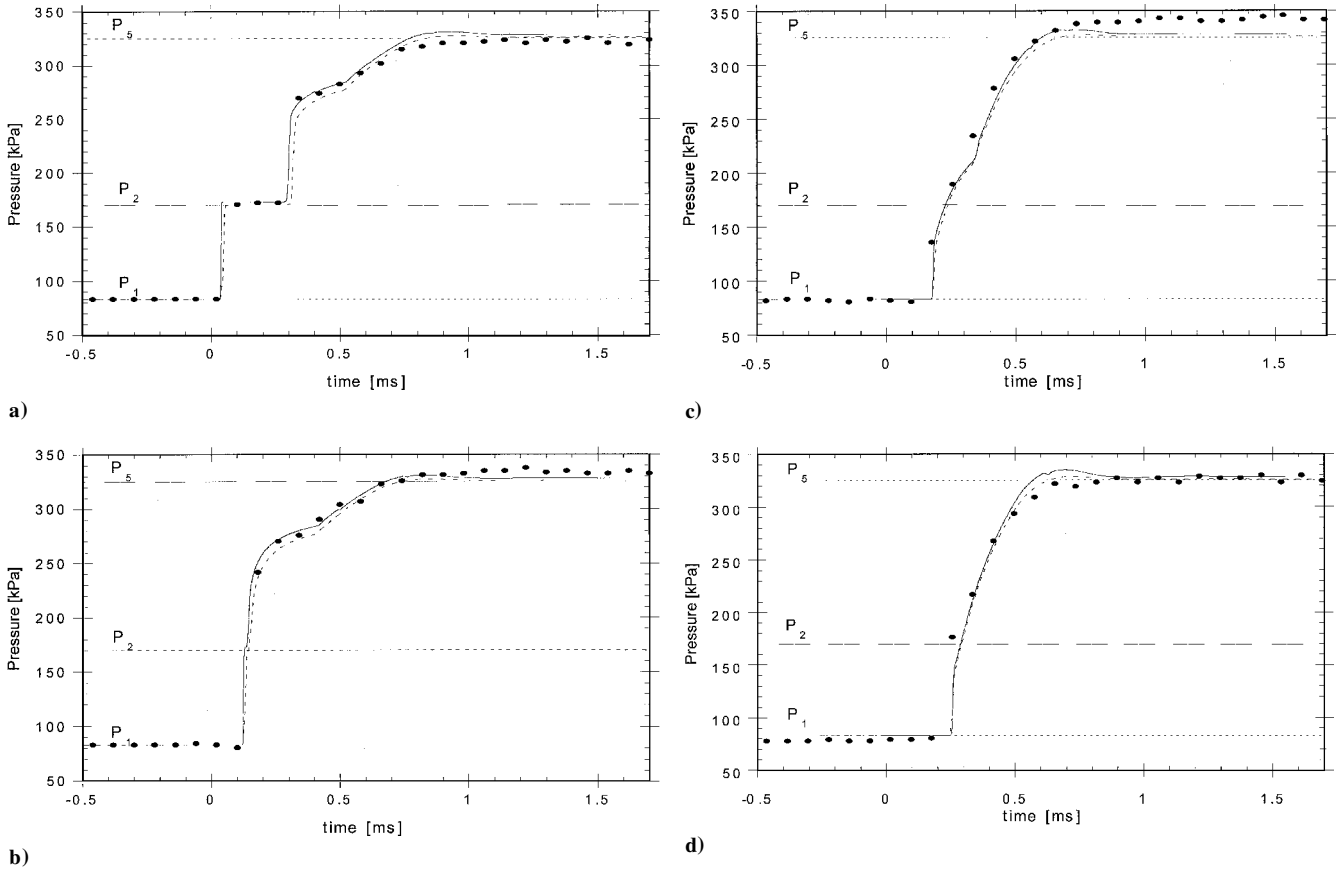

Fig. 4 Comparison between the predictions of the present two-dimensional ALE numerical simulations and both the experimental data and the one-dimensional TVD numerical simulations of Ref. 7 for the pressure histories of the gas for the head-on interaction of a shock wave with a 40-mm SiC porous sample. The incident shock-wave Mach number was 1.378. The pressure histories of the gas upstream and 3 mm upstream from the front edge of the porous sample are shown in panels a and b, respectively (ports 4 and 6 in Fig. 3, respectively), and the pressure histories of the gas occupying the pores of the porous material along the shock tube side wall and at its end wall are shown in panels c and d, respectively (ports 7 and 8 in Fig. 3, respectively): symbols and – – –, the experimental data and the predictions of the one-dimensional TVD-based simulations of Ref. 7, respectively; and ——, the predicted values of the present two-dimensional ALE numerical simulations at the center of the shock-tube cross section.

be presented. In all of the simulations, the grid resolutions were 0.25 mm per numerical cell in a square mesh.

A. Comparison with Numerical Simulation and Experimental Data: One-Dimensional Case

The first assessment of the two-dimensional numerical code was to check its performance by numerically simulating the head-on collision of a shock wave with a rigid porous material and comparing its predictions with both experimental data[11] and the predictions of a one-dimensional total-variation-diminishing (TVD)-based numerical code.[7] The shock-tube experimental setup and the location of pressure transducers are shown in Fig. 3. During these simulations, it was assumed that the shock-tube end wall is rigid, whereas the shock-tube side walls considered being infinite boundaries. Rigid porous samples made of silicon carbide (SiC) were mounted at the shock-tube test section. Their rear edge was supported by the shock-tube end wall. Table 1 represents both the initial conditions and the physical properties of the samples for two typical cases, which were chosen to assess both the model and the numerical code.[7] Typical results of the experimental study of Ref. 11 and the numerical simulations of both the one-dimensional TVD code of Ref. 7 and our two-dimensional ALE code for 40- and 60-mm-long samples made of SiC are presented in Figs. 4 and 5, respectively. The incident shock-wave Mach numbers in these experiments were 1.378 and 1.385, respectively. The pressure histories of the pure gas upstream of the test section and at the front edge of the porous material are shown in Figs. 4a, 5a, 4b, and 5b, respectively. The pressure histories of the gas occupying the pores of the porous material along the test section side wall and at the shock tube end wall are shown in Figs. 4c, 5c, 4d, and 5d, respectively. The symbols and the dashed lines represent the experimental data and the predictions of the one-dimensional TVD-based simulations of Ref. 7. The solid lines represent the predicted values of the present ALE two-dimensional numerical simulations at the center of the shock-tube cross section. In these figures P_1 is the pressure ahead of both the incident and the transmitted shock waves, P_2 is the theoretical pressure that should have been reached behind the incident shock wave, and P_5 is the theoretical pressure that should have been reached had the incident shock wave reflected head on from a solid end wall.

Table 1 Initial conditions and material properties of the silicon carbide for the head-on collision experiments[7]

Figure No.	M_i	T_0,[a] k	P_0,[b] kPa	Sample length, mm	Forchheimar constant	Porosity	Tortuosity
4	1.378	290	83.04	40	300	0.8	0.7
5	1.385	290	83.11	60	500	0.8	0.7

[a] T_0 = initial temperature before incident shock wave.
[b] P_0 = pressure before incident shock wave.

It is evident from these comparisons that the agreement between the predictions of our two-dimensional ALE numerical simulation with both the experimental results and the one-dimensional TVD code of Ref. 7 is very good. The present ALE two-dimensional numerical simulations reproduced the pressure histories of the gaseous phase both inside and outside of the SiC porous sample and for 40- and 60-mm-long samples (Figs. 4 and 5, respectively). Very good agreement is evident in the rates of pressure rise for both models. This indicates that the ALE numerical code predicts correctly the specimen length influence upon the gas flowfield and therefore can be implemented in future as a two-phase code.

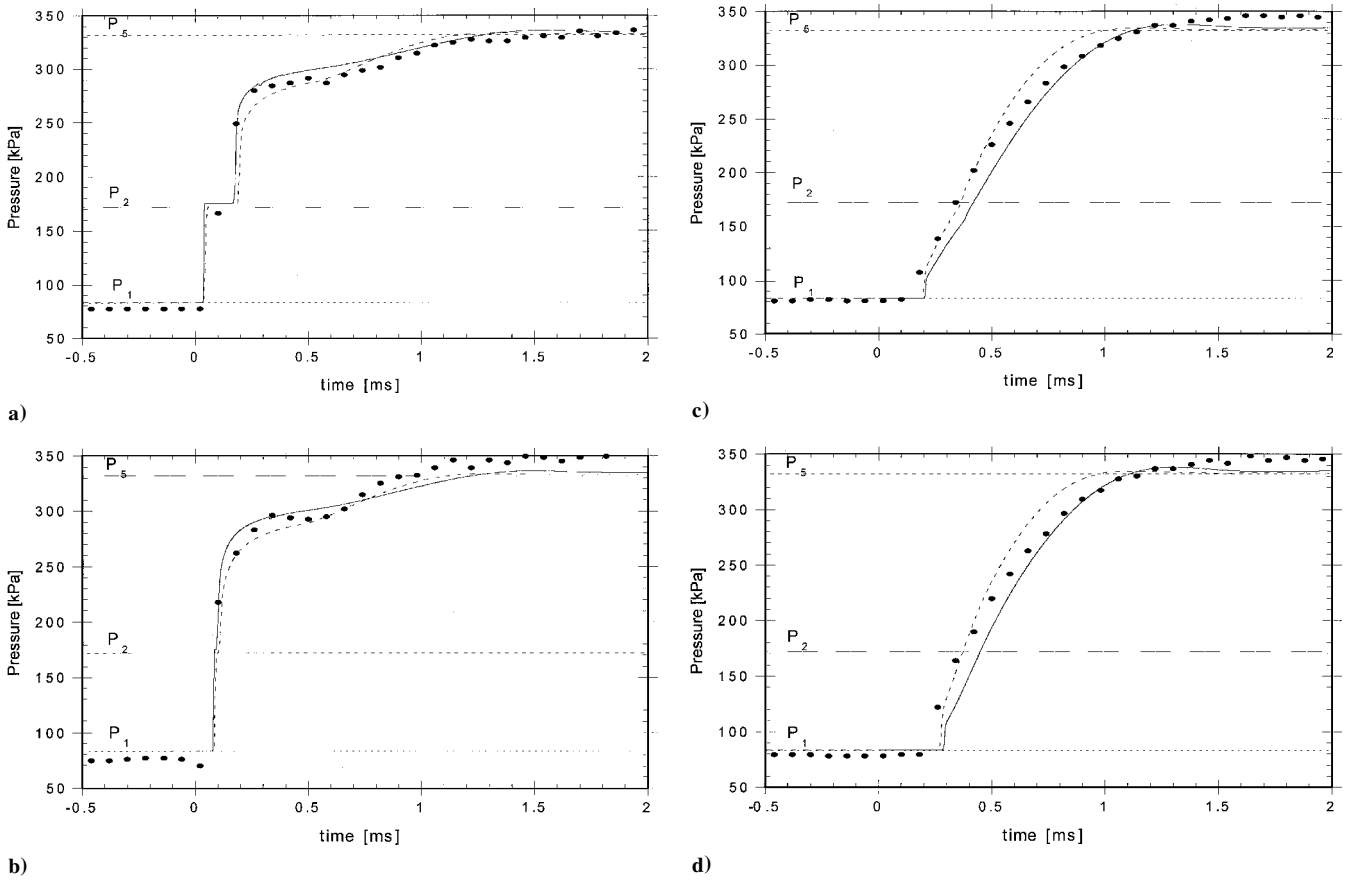

Fig. 5 Comparison between the predictions of the two-dimensional ALE numerical simulations and both the experimental data and the one-dimensional TVD numerical simulations of Ref. 7 for the pressure histories of the gas for the head-on interaction of a shock wave with a 60-mm SiC porous sample. The incident shock-wave Mach number was 1.385. The pressure histories of the gas upstream and at the front edge of the porous sample are shown in panels a and b, respectively (ports 4 and 5 in Fig. 3, respectively), and the pressure histories of the gas occupying the pores of the porous material along the shock-tube side wall and at its end wall are shown in panels c and d, respectively (ports 7 and 8 in Fig. 3, respectively): symbols and – – –, the experimental data and the predictions of the one-dimensional TVD-based simulations of Ref. 7, respectively; and ——, the predicted values of the present two-dimensional ALE numerical simulations at the center of the shock-tube cross section.

Table 2 Comparison between the predictions of the analytical model[13] and numerical simulation results of the pressure and the density values at the various uniform zones (see Fig. 1)

	Pressure, kPa, at flow zone:				Density, kg/m^3, at flow zone:			
Physical property	4	3	2	1	4	3	2	1
Analytical model	126.3	126.3	126.3	125.6	1.343	1.344	1.344	1.338
Numerical simulation	124.1	124.0	124.2	124.6	1.350	1.360	1.360	1.340
Difference, %	1.74	1.82	1.66	0.8	0.45	1.2	1.2	0.12

B. Comparison with Predictions of Analytical Model and Experimental Data: Two-Dimensional Case

Based on the good numerical predictions of the presently developed code in the case of a one-dimensional shock-wave interaction, we felt confident enough to move forward and simulate the oblique reflection of planar shock wave over rigid porous surface using our two-dimensional ALE numerical model. Wall boundary conditions were assumed at the shock-tube walls that supported the edges of the porous sample. Otherwise, infinite boundaries were assumed.

1. Regular Reflection over a Rigid Porous Surface

As a first step, the developed code was used to predict the wave configuration and the flowfield characteristics of a regular reflection over a rigid porous surface. The wave configuration for this case and the definitions for the various uniform zones associated with the flowfield (as suggested in Ref. 12) are shown in Fig. 1.

Comparison between the predictions of the numerical simulations and the predictions of the two-dimensional analytical model[13] for the RR of an oblique shock wave over a rigid porous surface in pseudosteady flows is presented in Table 2. In this case the incident shock wave Mach number was 1.2, the reflecting wedge angle was 30 deg, and the porosity was 0.98. The prediction of the numerical simulations revealed that the uniform zones associated with the flow characteristics are not as uniform, as was suggested in Fig. 1, especially far away from the reflection point and inside the porous medium. Hence, average values for the gas pressure and density were taken near the reflection point. These average values are presented in Table 2. It can be clearly seen in Table 2 that the differences between the predictions of our two-dimensional ALE numerical simulation and Li et al.'s analytical model[13] are very small. Unlike Li et al.'s analytical model,[13] which can only be used to predict the regular reflection of an oblique shock wave from a rigid porous surface and whose solution is limited to the area in the vicinity of the reflection point, the proposed two-dimensional ALE model can predict the flow characteristics of any two-dimensional interaction of a planar shock wave with a porous medium and at any point in the investigated flowfield.

Kobayashi et al.[12] investigated experimentally the regular reflection of a shock wave over a porous surface and measured the reflection angle ω_r as a function of the incident shock wave angle ω_i (for definition of ω_r and ω_i; see Fig. 1). Their results for an incident shock wave having a Mach number 1.2 are presented in Fig. 6. The dashed line describes the relation between ω_r and ω_i as obtained by the two-shock theory[19] for the reflection over a solid plain wall (i.e., a wall with zero porosity, $\phi = 0$). The dashed–dotted line describes the other limiting case of $\phi = 1$. Hence the relation between ω_r and ω_i for any porous material ($0 < \phi < 1$) should lie in between these two limiting lines. The experimental results marked by the triangles and the squares were obtained over a dusty layer having porosities of $\phi = 0.44$ and 0.98, respectively. The predictions of the two-dimensional numerical simulations are shown in Fig. 6 by solid lines. The values of the numerical reflected angle ω_r were obtained via a graphical averaging process after an enlargement the area in the vicinity of the refection point. As can be seen, very good to excellent agreement was obtained for both cases.

The regular reflections of oblique shock wave from rigid porous wedges for wedge angles 30 and 50 deg are shown in Figs. 7 and 8, respectively. The predictions of the gas pressure and density fields for a regular reflection over rigid porous wedges are shown in Figs. 7a and 8a and 7b and 8b, respectively. Schlieren photograph of a regular reflections under the same conditions[20] are shown in Figs. 7c and 8c. The obtained RR wave configuration is similar to that proposed

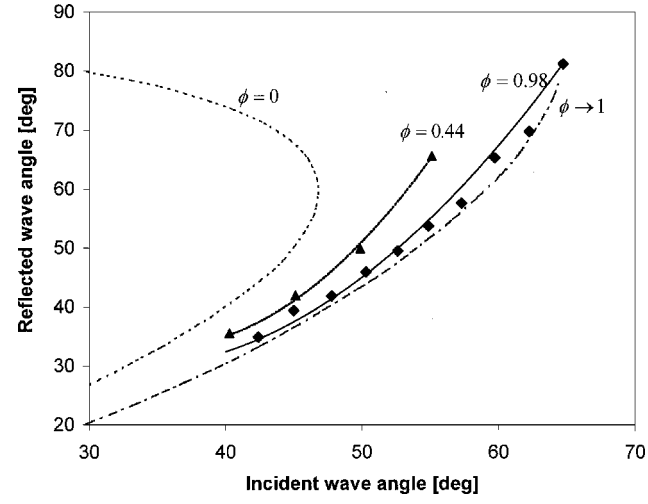

Fig. 6 Reflected shock-wave angle ω_r as a function of the incident shock wave angle ω_i for $M_i = 1.2$ and the porosity $\phi = 0.44$ and 0.98: – – –, the relation between ω_r and ω_i as obtained by the two-shock theory[19] for the reflection over a solid plain wall (i.e., a wall with zero porosity, $\phi = 0$), and –·–, the other limiting case of $\phi = 1$.

by Ref. 12 and shown in Fig. 1. The incident and the transmitted waves are clearly seen. Unlike the incident shock wave, which remained straight as it propagated downstream, the transmitted wave developed a backward curvature (change in the shock wave slope), near the interface between the gas and the porous layer, as a result of the internal geometrical structure of the wedge and multiple reflections caused by the solid material. As the wedge depth increased, the propagation length of the transmitted wave increased. Therefore because of macroscopic internal friction and multiple reflections the transmitted wave became more dispersed. As was suggested by Kobayashi et al.[12] in Fig. 1, a slipstream inside the porous wedge was formed (Figs. 7a and 8a) as a result of the mass transfer into the porous layer. The slipstream became dispersed as it propagated through the porous medium. It can also be seen that both the pressure and the density are not uniform behind the reflected wave. Similar observation was obtained experimentally by Ref. 20 (Figs. 7c and 8c). This might be because of the multiple reflections from the porous surface as was reported by Ref. 11 for the one-dimensional interaction and because of the reflection of the transmitted shock wave from the rigid boundary wall. The reflection of the transmitted shock wave from the rigid boundary wall depends on the curvature of the transmitted wave. When the wedge angle is large, as is the case shown in Fig. 8, the distance between the reflection point of the incident shock wave and the reflection point of the transmitted shock wave from the rigid boundary wall is large. As a result, the curvature of the transmitted wave decreases, and the reflection of the transmitted shock wave from the rigid boundary wall is less noticeable. However, when the distance between those reflection points is short, as is the case for the small wedge angle (Fig. 7), the reflection from the rigid wall is well noticed near the wall. The reflected wave then becomes dispersed as it propagates backwards. Note that, for this case, the transmitted shock wave reflects as a MR from the rigid solid wall.

The comparison between the prediction of the numerical simulations, shown in Figs. 7a and 7b and 8a and 8b, and the experimental results of Skews,[20] shown in Figs. 7c and 8c, showed that very good agreements were obtained for the values of the numerical reflected angle ω_r.

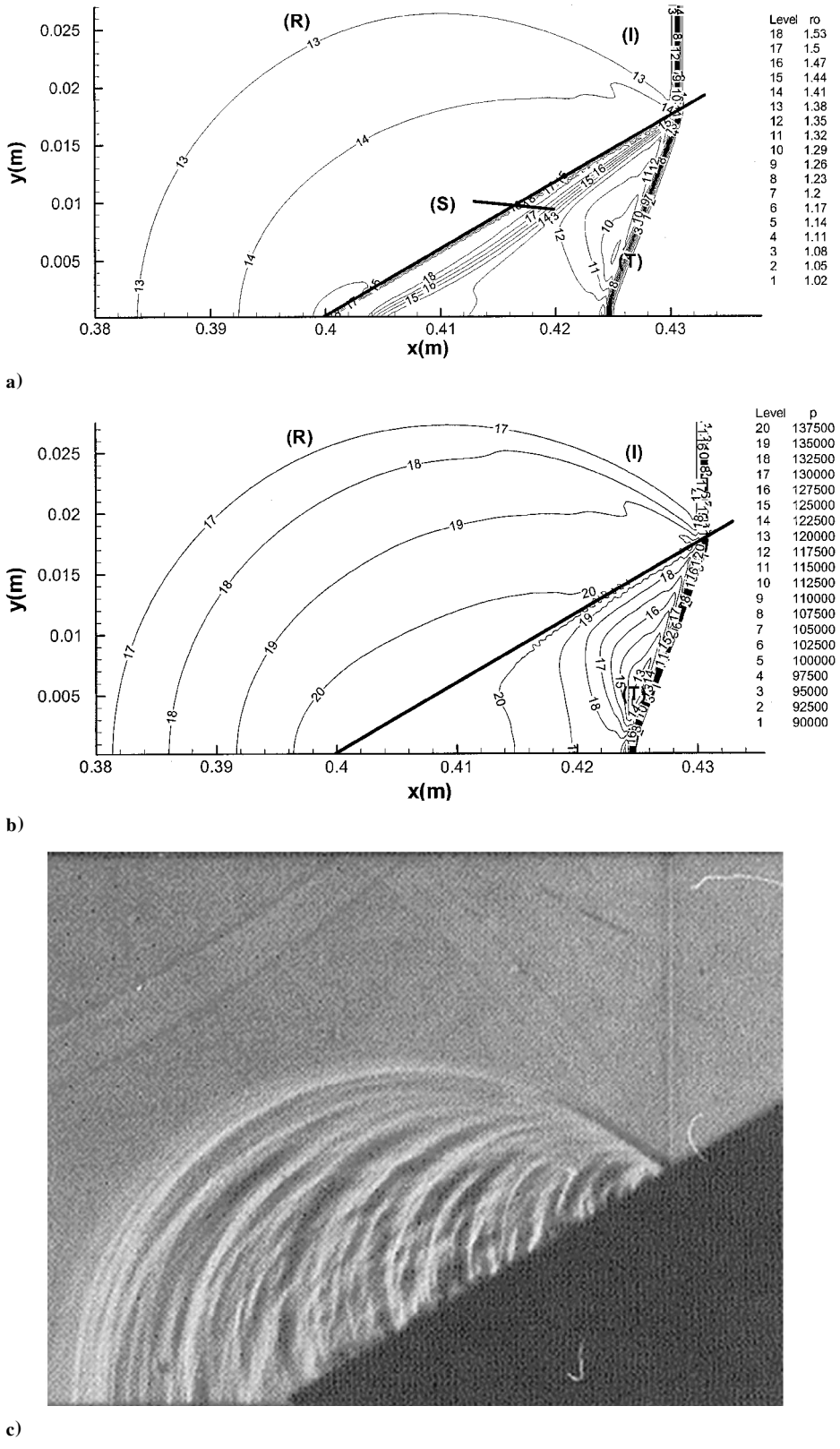

Fig. 7 Predictions of the gas density, pressure fields (two-dimensional ALE numerical simulation), and a schlieren photograph[20] (panels a–c, respectively) for a regular reflection from a rigid porous wedge. The incident shock-wave Mach number was 1.22, the wedge angle was 30 deg, and the porosity was 0.73: *I*, the incident shock wave; *T*, the transmitted shock wave; *R*, the reflected shock wave; and *S*, the slipstream.

2. Irregular Reflection over a Rigid Porous Medium

Following the validation of the numerical code by assessing its predictions for the RR case, including inside the porous medium, we felt confident to take the next step and simulate a more complex reflection phenomenon, that is, a IR over a rigid porous medium. Generally, the IR can be divided into two major categories: von Neumann reflection (vNR) and MR. The MR wave configuration consists of three shock waves (namely, incident, reflected, and Mach stem) and one slipstream. Colella and Henderson[21] found that there are some cases in which the reflected shock wave degenerates into a compression wave near the triple point and named the reflection phenomena in these cases as von Neumann reflection. To the best of the authors' knowledge the IR over a rigid porous medium has never been solved analytically or numerically.

Figure 9 presents the prediction of the numerical simulations and the experimental results of Skews[20] for an irregular reflection

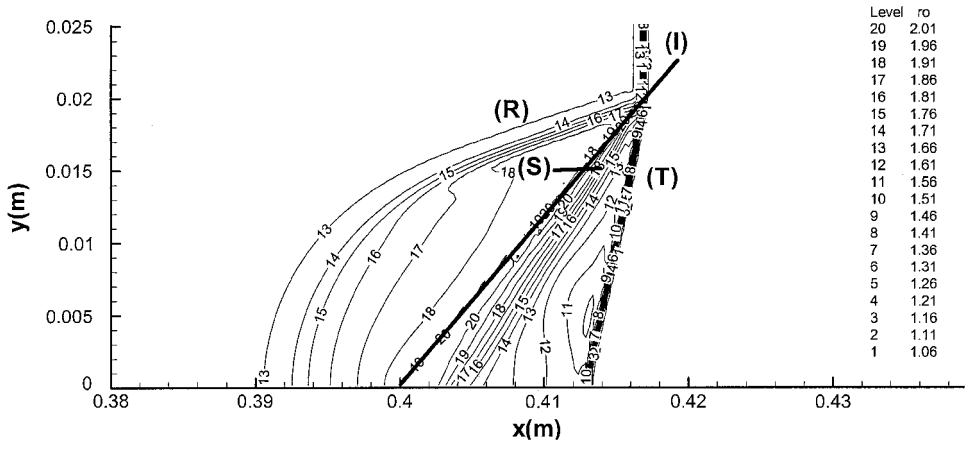

a)

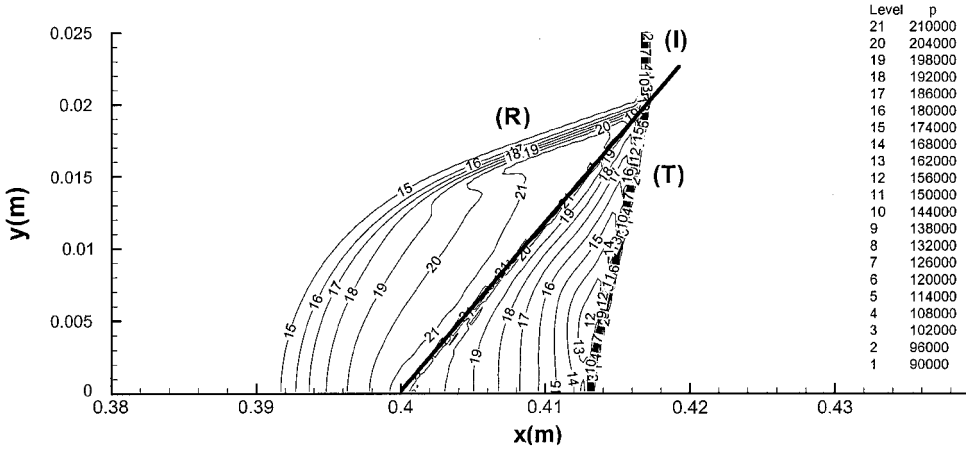

b)

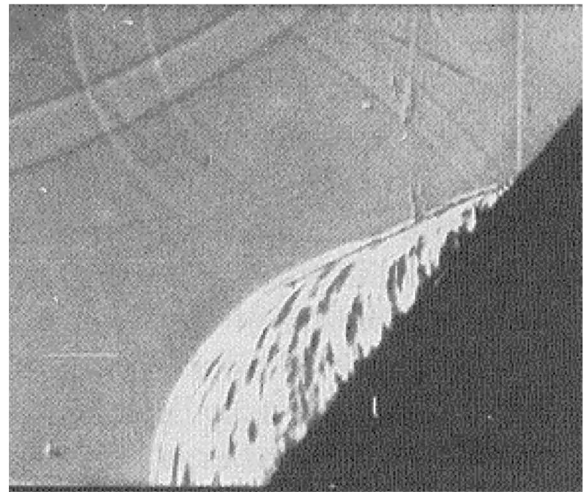

c)

Fig. 8 Predictions of the gas density, pressure fields (two-dimensional ALE numerical simulation), and a schlieren photograph[20] (panels a–c, respectively) for a regular reflection form a rigid porous wedge. The incident shock-wave Mach number was 1.37, the wedge angle was 50 deg, and the porosity was 0.73: *I*, the incident shock wave; *T*, the transmitted shock wave; *R*, the reflected shock wave; and *S*, the slipstream.

from a rigid porous wedge. Although this reflection may term as a vNR, it was described by Skews[20] as Mach reflection. The incident shock-wave Mach number was 1.53, and the wedge angle was 10 deg. Comparison between the prediction of the numerical simulations, shown in Figs. 9a and 9b, and the experimental results of Skews,[20] shown in Fig. 9c, revealed that the simulation successfully reproduced the IR configuration. Both the numerical prediction and Skews's observation showed that the Mach stem was curved backwards and lagged behind the incident wave in contrast to the reflection over a solid nonporous surface. In addition, a clear triple point was not noticeable at all. Hence, it can be concluded that the MR wave configuration as proposed and shown in Fig. 2 does not describe the numerically and the experimentally obtained IR wave configuration correctly for the specific initial parameters that were studied in this paper. It is also clearly shown in the numerical prediction (Fig. 9a) that the slipstream emanating from the triple point was not formed, or was covered up by the reflected waves emerging from the porous media. Because of the Mach stem curvature and the slipstream absence, we refer the wave configuration shown in Fig. 9 as IR rather than vNR. However, the physical phenomena inside the porous material include the same elements shown for the RR case, including the transmitted shock interaction with the rigid boundary

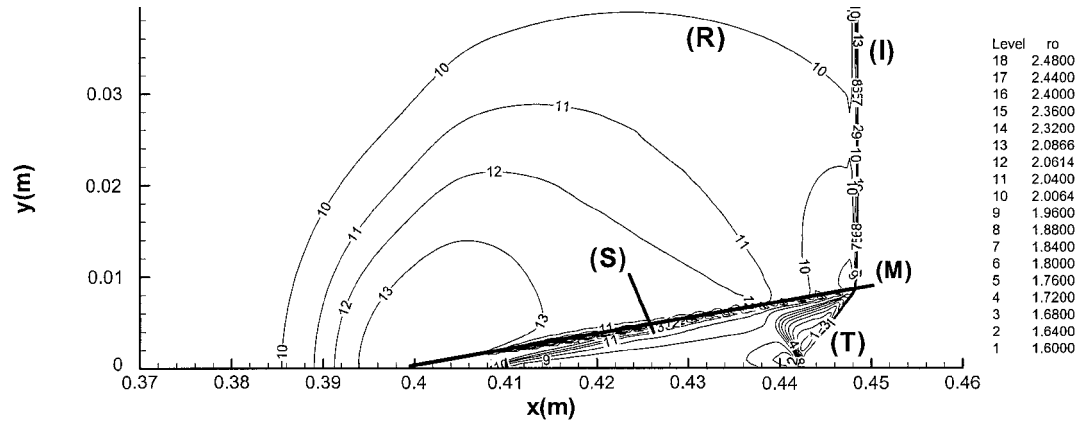

a)

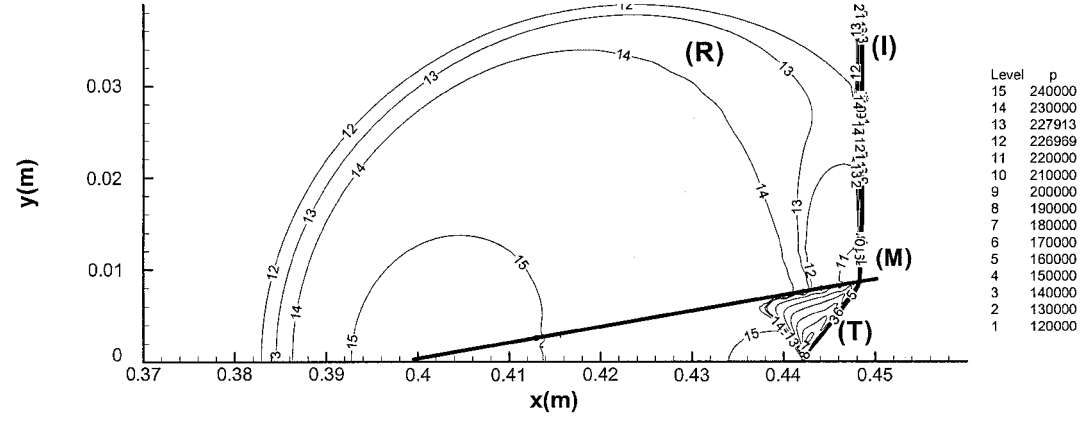

b)

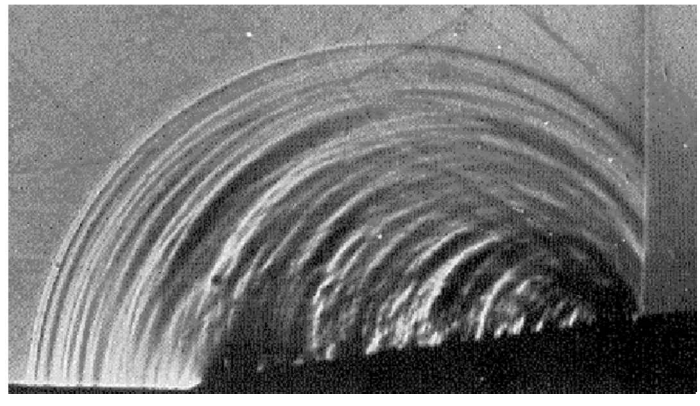

c)

Fig. 9 Predictions of the gas density, pressure fields (two-dimensional ALE numerical simulation), and a schlieren photograph[20] (panels a–c, respectively) for an irregular reflection form a rigid porous wedge. The incident shock-wave Mach number was 1.53, the wedge angle was 10 deg, and the porosity was 0.73: *I*, the incident shock wave; *T*, the transmitted shock wave; *R*, the reflected shock wave; and *S*, the slipstream. The backward-curving Mach stem (M) is not so clear.

wall. The transmitted shock wave reflects as a MR over the rigid boundary wall. The reflected wave resulting from this internal reflection propagates backward and finally emerges out of the porous surface.

The comparison between the prediction of the numerical simulations, shown in Figs. 9a and 9b, and the experimental results of Skews,[20] shown in Fig. 9c, showed that very good agreements were obtained for the numerical reflected wave curvature, not only close to the vicinity of the triple point.

V. Conclusions

A two-dimensional numerical model capable of predicting the characteristics of the flowfield during the unsteady interaction of shock waves with rigid saturated porous materials has been developed. The predictions of the numerical simulations were successfully compared with the predictions of the two-dimensional analytical model[13] for the case of a regular reflection from a rigid porous surface in pseudosteady flow. Comparisons between the predictions of the numerical simulations with the one-dimensional numerical and experimental results of Ref. 11 and with the two-dimensional experimental data of Ref. 12 confirmed the validity of the physical model and the numerical code. In addition, the comparison between the predictions of the two-dimensional numerical simulations and the experimental data of Ref. 20 confirmed the validity of the code for both RR and IR waves configurations. Although the predictions of the numerical model for the RR and the IR were validated by the flowfield outside the porous material, to best of the authors' knowledge, this is the first time that the flowfield characteristics inside the porous material, which resulted from the interaction of oblique shock waves with porous wedges, were predicted. In addition, it is the first time that the IR configuration over a porous surface has been solved. In a future study similar concepts will be used to simulate the reflection phenomenon over compressible porous materials (e.g., polyurethane foams, etc.).

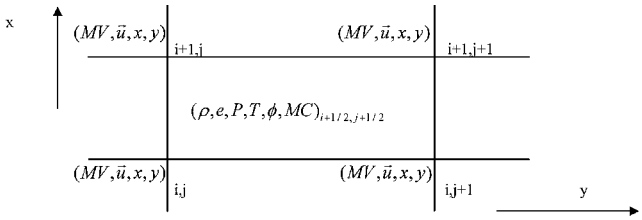

Fig. A1 Numerical grid. The scalar properties are located inside the cell (with the exception of the vertex mass, which is needed for vertex acceleration calculations), and the vectors are located in the vertices. MV is the vertex mass and MC is the cell mass.

Appendix: Numerical Scheme

The numerical code adopted the leapfrog method.[22] This method was implemented by using two types of time steps, the larger one for the primary physical properties and the smaller one for the derivatives of the primary properties. For example, a vertex coordinate is presented at the larger time steps, whereas the vertex speed is presented at the smaller time steps. The definitions of the location of the physical properties on the numerical grid are shown in Fig. A1. As can be seen, all of the scalar physical properties were defined on the center of each numerical cell, and all of the vector properties (i.e., velocity) were defined at the vertices. In addition to the cell mass (MC), the vertex mass (MV) was also defined in order to calculate the vertex acceleration and the new location.

When a Lagrangian method, which is based on fixed mass elements, is used, there is no need to solve the mass balance equation because it is conserved by the scheme definitions. Each cell (numerical element) has a fixed mass, which is defined by its initial conditions and is calculated from

$$m_{i+\frac{1}{2},j+\frac{1}{2}} = (\rho V)^0_{i+\frac{1}{2},j+\frac{1}{2}} \tag{A1}$$

where the superscript 0 refers to the initial reference time. Thus the calculation starts with solving the momentum equation to get the new velocity and location of each vertex. The new cell density is then calculated from the new volume of the cell that can be calculated from the partial difference of the cell vertices:

$$\rho^{n+1}_{i+\frac{1}{2},j+1,2} = \frac{m_{i+\frac{1}{2},j+\frac{1}{2}}}{V^{n+1}_{i+\frac{1}{2},j+1,2}} \tag{A2}$$

The calculation procedure of the accelerations and the velocities has a combined effect of pressure and artificial viscosity on the vertices momentum. Using Newton's second law, the vertex acceleration can be calculated by dividing these two force elements by the vertex mass. The vertex mass was calculated from

$$MV = 0.5\sum_{k=1}^{4} A_k \rho_k \tag{A3}$$

where the subscript k represents the four cells around the vertex, ρ is the cell density, and A is a triangle area as shown in Fig. A2. The vertex mass can be also calculated by a simple average of the four neighbor cells, but this way is not effective because it can cause an unsteady solution performance in a simple Lagrangian procedure that includes high cell strains.

The derivatives of the vertex velocity were calculated from

$$\mathrm{d}(u_x)^{n+\frac{1}{2}}_{i,j} = -\frac{\mathrm{d}t_2}{2MV^n_{i,j}}\left[\sum_{2'}^{n}\Delta y^n_{32} + \sum_{1'}^{n}\Delta y^n_{21} + \sum_{3'}^{n}\Delta y^n_{43} + \sum_{4'}^{n}\Delta y^n_{14}\right] - \mathrm{d}t_2 S_2^{n-\frac{1}{2}} \tag{A4}$$

$$\mathrm{d}(u_y)^{n+\frac{1}{2}}_{i,j} = -\frac{\mathrm{d}t_2}{2MV^n_{i,j}}\left[\sum_{2'}^{n}\Delta x^n_{32} + \sum_{1'}^{n}\Delta x^n_{21} + \sum_{3'}^{n}\Delta x^n_{43} + \sum_{4'}^{n}\Delta x^n_{14}\right] - \mathrm{d}t_2 S_3^{n-\frac{1}{2}} \tag{A5}$$

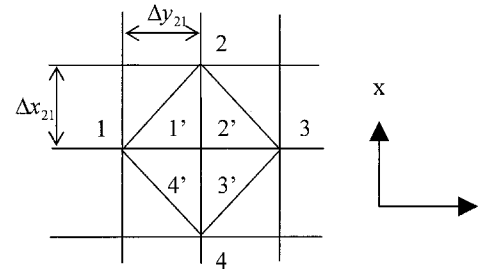

Fig. A2 Procedure for calculating the vertex mass.

where $\sum$ is calculated from

$$\sum_{k}^{n} = \left(P^n_k + q^{n-\frac{1}{2}}_k\right) \tag{A6}$$

The subscripts 1′–4′ of P and 1–4 of Δx and Δy represent the values of the pressure located at the neighbor cells and the coordinates difference of x and y, respectively (Fig. A2).

The cell internal energy was calculated from

$$e^{n+1}_{i+\frac{1}{2},j+\frac{1}{2}} = e^n_{i+\frac{1}{2},j+\frac{1}{2}} - \frac{1}{MC^n_{i,j}}\left(\hat{P} + q^{n+\frac{1}{2}}_{i+\frac{1}{2},j+\frac{1}{2}}\right)\Delta V + \mathrm{d}t \cdot S_4^{n-\frac{1}{2}} \tag{A7}$$

In this equation $q^{n+1/2}_{+1/2i,j+1/2}$ is the calculated artificial viscosity of the cell and $\hat{P}$ is the time average of the cell pressure. To simplify the pressure work integral, the time-averaged pressure should be calculated at the time $n+\frac{1}{2}$. Because the internal energy and the pressure are dependent variables of the equation of state, the time-averaged pressure was calculated using the following procedure:

$$\hat{P}^{n+\frac{1}{2}} = \tfrac{1}{2}(P^{n+1} + P^n) \tag{A8}$$

where the pressure P^{n+1} was calculated by a first-order approximation:

$$P^{n+1} = P^n + \left(\frac{\partial P^n}{\partial e^n}\right)_\rho \Delta e + \left(\frac{\partial P^n}{\partial \rho^n}\right)_e \Delta\rho \tag{A9}$$

The partial derivatives of the pressure were defined by differentiating the equation of state:

$$\left(\frac{\partial P}{\partial e}\right)_\rho = (\gamma - 1)\rho \tag{A10}$$

$$\left(\frac{\partial P}{\partial \rho}\right)_e = (\gamma - 1)e \tag{A11}$$

Linear and quadratic terms were accounted for in the artificial viscosity q, which was calculated from

$$q^{n+\frac{1}{2}}_{i+\frac{1}{2},j+\frac{1}{2}} = \rho^n_{i+\frac{1}{2},j+\frac{1}{2}} L\left[C_0 L D^{n-\frac{1}{2}}_{i+\frac{1}{2},j+\frac{1}{2}} - C_L c^n_{i+\frac{1}{2},j+\frac{1}{2}}\right] \times \min\left[0, D^{n-\frac{1}{2}}_{i+\frac{1}{2},j+\frac{1}{2}}\right] \tag{A12}$$

$$D = \frac{\partial u_x}{\partial x}\cos^2(\alpha) + \frac{\partial u_y}{\partial y}\sin^2(\alpha) + \left(\frac{\partial u_x}{\partial y} + \frac{\partial u_y}{\partial x}\right)\cdot\cos(\alpha)\sin(\alpha) \tag{A13}$$

In these equations D is the general expression of the velocity divergence, L is the average string of the cell, c is the local speed of sound in the cell, and α is the angle between the x axis and the direction of propagation of the shock inside the cell. The constants C_L and C_0 were determined as 0.15 and 0.05, respectively, in order to reach the highest resolution and a stable solution performance.

After each time step a remesh procedure was implemented. The procedure included the following steps: 1) calculation of the new grid coordinates, 2) volume advection between the old grid to the new grid (the Eulerian grid), 3) transfer of physical properties between the old grid to the new grid, and 4) updating the velocity vectors on the new grid.

References

[1]Ben-Dor, G., *Shock Wave Reflection Phenomena*, Springer-Verlag, New York, 1991.

[2]Ben-Dor, G., Igra, O., and Elperin, T., *Handbook on Shock Waves*, Academic Press, Boston, 2000.

[3]Baer, M. R., "A Numerical Study of Shock Wave Reflections on Low Density Foam," *Shock Waves*, Vol. 2, No. 2, 1992, pp. 121–124.

[4]Bear, J., Sorek, S., Ben-Dor, G., and Mazor, G., "Displacement Waves in Saturated Thermoelastic Porous Media. I. Basic Equations," *Fluid Dynamics Research*, Vol. 9, No. 1–3, 1992, pp. 155–164.

[5]Levy, A., Sorek, S., Ben-Dor, G., and Bear, J., "Evolution of the Balance Equations in Saturated Thermoelastic Porous Media Following Abrupt Simultaneous Changes in Pressure and Temperature," *Transport in Porous Media*, Vol. 21, No. 3, 1995, pp. 241–268.

[6]Levy, A., Sorek, S., Ben-Dor, G., and Skews, B., "Wave Propagation in Saturated Rigid Porous Media: Analytical Model and Comparison with Experimental Results," *Fluid Dynamics Research*, Vol. 17, No. 2, 1996, pp. 49–65.

[7]Levy, A., Ben-Dor, G., and Sorek, S., "Numerical Investigation of the Propagation of Shock Waves in Rigid Porous Materials: Development of the Computer Code and Comparison with Experimental Results," *Journal of Fluid Mechanics*, Vol. 324, 1996, pp. 163–179.

[8]Skews, B. W., Levy, A., and Levi-Hevroni, D., "Shock Wave Propagation in Porous Media," *Handbook on Shock Waves*, edited by G. Ben-Dor, O. Igra, and T. Elperin, Academic Press, Boston, 2000.

[9]Sorek, S., Bear, J., Ben-Dor, G., and Mazor, G., "Shock Waves in Saturated Thermoelastic Porous Media," *Transport in Porous Media*, Vol. 9, No. 1–2, 1992, pp. 3–13.

[10]Levi-Hevroni, D., "Non-Linear Waves Propagation in Multiphase Porous Media," Ph.D. Dissertation, Dept. of Mechanical Engineering, Ben-Gurion Univ. of the Negev, Beer-Sheva, Israel, May 2000.

[11]Levy, A., Ben-Dor, G., Skews, B. W., and Sorek, S., "Head-on Collision of Normal Shock Waves with Rigid Porous Materials," *Experiments in Fluids*, Vol. 15, 1993, pp. 183–190.

[12]Kobayashi, S., Adachi, T., and Suzuku, T., "Regular Reflection of a Shock Wave over a Porous Layer: Theory and Experiment," *Shock Waves @ Marseille IV*, edited by R. Brun and L. Z. Dumitrescu, Springer-Verlag, Berlin, 1995, pp. 175–180.

[13]Li, H., Levy, A., and Ben-Dor, G., "Analytical Prediction of Regular Reflection over Rigid Porous Surfaces in Pseudo-Steady Flow," *Journal of Fluid Mechanics*, Vol. 282, 1995, pp. 219–232.

[14]Skews, B. W., "Oblique Reflection of Shock Waves from Rigid Porous Material," 10th Mach Reflection Symposium, Denver, CO, June 1992.

[15]Bear, J., and Bachmat, Y., *Introduction to Modeling of Transport Phenomena in Porous Media*, Kluwer Academic, Dordrecht, The Netherlands, 1990.

[16]Levy, A., Levi-Hevroni, D., Sorek, S., and Ben-Dor, G., "Derivation of Forchheimer Terms and Their Verification by Application to Compaction Waves Propagation in Porous Media," *International Journal of Multiphase Flow*, Vol. 25, No. 4, 1999, pp. 683–704.

[17]Levy, A., Ben-Dor, G., and Sorek, S., "Numerical Investigation of the Propagation of Shock Waves in Rigid Porous Materials—Flow Field Behavior and Parametric Study," *Shock Waves*, Vol. 8, No. 3, 1998, pp. 127–137.

[18]Wilkins, M. L., "Calculations of Elastic Plastic Flow," *Methods in Computational Physics III*, Academic Press, New York, 1964, pp. 211–247.

[19]von Neuman, J., "Oblique Reflection of Shocks," Explosive Research Rept. 12, Bureau of Ordnance, Navy Dept., Washington DC, 1943.

[20]Skews, B. W., "Oblique Reflection of Shock Waves from Rigid Porous Materials," *Shock Waves*, Vol. 4, No. 3, 1994, pp. 145–154.

[21]Colella, P., and Henderson, L. F., "The von Neumann Paradox for the Diffraction of Weak Shock Waves," *Journal of Fluid Mechanics*, Vol. 213, 1990, pp. 71–94.

[22]Courant, R., Friedrichs, K. O., and Lewy, H., "On the Partial Difference Equations of Mathematical Physics," *IBM Journal of Research and Development*, Vol. 11, No. 2, 1967, pp. 215–234.

M. Sichel
Associate Editor